https://doi.org/10.5194/egusphere-2023-1546
Preprint. Discussion started: 16 October 2023

Rotary-wing drone-induced flow – comparison of simulations with lidar measurements

Liqin Jin[1, *], Mauro Ghirardelli[2, *], Jakob Mann[1], Mikael Sjöholm[1], Stephan T. Kral[3], and Joachim Reuder[2, 3]

[1]Department of Wind and Energy Systems, Technical University of Denmark, Frederiksborgvej 399, 4000 Roskilde, Denmark.
[2]Geophysical Institute and Bergen Offshore Wind Centre, University of Bergen, 5020 Bergen, Norway
[3]Geophysical Institute and Bjerknes Centre for Climate Research, University of Bergen, 5020 Bergen, Norway
[*]These authors contributed equally to this work.

Correspondence: Mauro Ghirardelli (mauro.ghirdelli@uib.no), Liqin Jin (liqn@dtu.dk)

Abstract. Ultrasonic anemometers mounted on rotary-wing drones have the potential to provide a cost-efficient alternative to the classical meteorological mast-mounted counterpart for wind energy applications. However, the propeller-induced flow may deteriorate the accuracy of free wind velocity measurements by wind sensors mounted on the drone. Therefore, we performed an experiment using three short-range continuous-wave Doppler lidars (DTU WindScanners) to measure the complex and turbulent three-dimensional wind field around a hovering drone at low ambient wind speeds. The results obtained by lidar measurements and computational fluid dynamics simulations are in good agreement. Both methods conclude that the disturbance zone on a horizontal plane 0.7 meters below the drone, extends about 2 meters upstream from the drone center for the horizontal wind velocity and more than 5 meters for the vertical wind velocity. By comparing wind velocities along horizontal lines in the upstream direction, we find that the velocity difference between the two methods is less than 0.1 ms^{-1} in most cases. Both plane and line scan results validate the reliability of simulations. Furthermore, simulations of flow patterns in a vertical plane at low ambient speed indicate that it is difficult to accurately measure the vertical wind component with less than 1% distortion by drone-mounted sonic anemometers.

1 Introduction

Wind energy has been growing rapidly in recent years and is now considered one of the best methods of reducing carbon emissions while supplying electricity (Luderer et al., 2017; Lazard, 2019). For wind turbines to operate efficiently, accurate characterization of wind conditions, i.e. wind velocity and direction, is crucial. As a powerful wind sensor, ultrasonic anemometers (sonics) have been used widely in wind energy. Compared to cup anemometers, sonic anemometers can determine all three components of the turbulent wind velocity with high accuracy (MacCready, 1966; Izumi and Barad, 1970), by measuring the ultrasonic waves' flight time along a path between two transducers (Kaimal et al., 1968). Additionally, compared to wind Doppler lidars (LIght Detection and Ranging), sonic anemometers are capable of responding to turbulent fluctuations of higher frequency (Bowen, 2007).

https://doi.org/10.5194/egusphere-2023-1546
Preprint. Discussion started: 16 October 2023

Traditionally, sonic anemometers are mounted on costly meteorological masts (met masts), providing single-point measurements. However, the diameter of the currently largest offshore wind turbines is close to 250 m with their blades sweeping vast areas bigger than several football fields. Consequently, the detailed characterization of wind fields over the entire rotor plane can no longer be based solely on the in-situ and single-point measurements by sonic anemometers. Besides, met-mast-based sonic measurements would be prohibitively expensive, especially for offshore wind farms. These hard realities underline the need to move beyond classical tower-based turbulence measurements.

Since the turn of the 21st century, rotary-wing drones have become more attractive in atmospheric measurements (Hemingway et al., 2017; Leuenberger et al., 2020; Tikhomirov et al., 2021). Their main advantages are cost-effectiveness, high-precision hovering, and ease of deployment and operation, which makes them a suitable platform for carrying various meteorological sensors (Abichandani et al., 2020), including anemometers (Prudden et al., 2016; Shimura et al., 2018; Thielicke et al., 2021; Li et al., 2023). The propeller-induced flow can, however, have a significant impact on wind measurements because each spinning propeller creates a disturbance in the flow that cannot be neglected when measuring wind.

One of the methods to reduce the influence of the propeller-induced flow is to mount the wind sensors away from the fuselage of the drone. This straightforward solution actually conceals some degree of difficulty. First of all, the flow is shown to depend on both internal factors, e.g. the drone's architecture and design (Guillermo et al., 2018; Lei and Cheng, 2020; Lei et al., 2020), and external factors, e.g. presence of walls, altitude above the ground, and wind conditions (Zheng et al., 2018; Lei and Lin, 2019; Guo et al., 2020). Secondly, adding weight far away from the center of gravity of the drone deteriorates its flight stability. Therefore, each drone-wind sensor pair configuration has specific quirks that need to be investigated.

The optimal placement of drone sensors requires a characterization of propeller-induced flow, which has been extensively studied by computational fluid dynamics (CFD). For reliable wind measurements, Wilson et al. (2022) suggested that a separation distance of 5.3 rotor diameters (5.3D) should be sufficient to minimize the propeller-induced flow when placing the sonic anemometer centered above the drone. Vasiljević et al. (2020) presented a proof-of-concept drone–lidar system to measure horizontal wind velocity with an agreement down to about 0.1 ms^{-1} compared to sonic anemometer data. They also concluded that the lidar should be placed out of the drone's disturbance zone stretching between 1 and 2 m from the center by measuring line-of-sight wind speed. In the current study, we experimentally validate a design simulation model for placing an upwind-facing, boom-mounted sonic anemometer below the fuselage. With such a configuration, an additional battery could be placed on the other side of the boom as a counterweight, which beneficially would prolong the flight duration.

Apart from simulations, high-resolution lidar remote sensing is a promising approach to experimentally investigate propeller-induced flow. Continuous-wave (CW) Doppler lidar can remotely obtain accurate three-dimensional flow observations without disturbing the flow. The spatial resolution of CW lidars diminishes with the focus distance, but they have higher spatial resolution than pulsed Doppler lidars within several hundred meters. Consequently, CW lidars are extensively applied to detect wind profiles (Köpp et al., 1984; Peña et al., 2009), assess wind resources (Bingöl et al., 2009; Sempreviva et al., 2008; Viselli et al., 2019), test wind turbines' performance based on wake measurements (Wagner et al., 2014; Shin and Ko, 2019; Fan et al., 2023), foresee the incoming gusts and flow to reduce loads (Bos et al., 2016), realize lidar-assisted turbine control to increase power production (Zhang and Yang, 2020; Guo et al., 2022), study turbulence around a suspension bridge (Cheynet

https://doi.org/10.5194/egusphere-2023-1546
Preprint. Discussion started: 16 October 2023

Figure 1. The Foxtech D130 x8, rotary-wing drone used in the experiment.

et al., 2016) and in the near-wake region of a tree (Angelou et al., 2022), with good spatial and temporal resolutions. Recently, two CW lidars were applied to measure the two-dimensional downwash wind fields in a horizontal and a vertical plane below a hovering search and rescue helicopter (Sjöholm et al., 2014).

Therefore, we conducted a field measurement campaign with three synchronized CW Doppler lidars to reconstruct the three-dimensional flow field around a drone for validating a CFD simulation set-up used to investigate the optimal sensor placement location for a sonic anemometer. Wind vectors obtained by lidars were compared with those resulting from the CFD simulations based on the setups presented by Ghirardelli et al. (2023). Such CFD setups have a relatively low computational cost since they rely on both geometrical simplification and ideal flow conditions, but they need to be validated. To the best of the authors' knowledge, this is the first study to use three CW lidars to investigate the turbulent three-dimensional flow around a rotary-wing drone.

In Section 2, the instruments and CFD simulations employed are elaborately described. Section 3 introduces the field measurement campaign and the wind characteristics obtained by a tower-mounted sonic anemometer nearby. The principle of Doppler spectral processing to retrieve wind vectors is presented in detail in Section 4 and the comparison of wind fields retrieved by the lidar measurements and CFD simulations is shown in Section 5. The most important findings of our study are summarized in the Conclusion (Section 6).

2 Instrumentation and model

2.1 The rotary-wing drone

The drone utilized in this study is the Foxtech D130 x8, a rotary-wing drone equipped with eight propellers arranged in four pairs of contra-rotating open rotors (Fig. 1). Each rotor has a diameter of 0.71 meters.

https://doi.org/10.5194/egusphere-2023-1546
Preprint. Discussion started: 16 October 2023

Each pair consists of two propellers spinning in opposite directions, driven by brushless electric motors (T-motor U10II KV100). The drone's take-off weight reaches 13.5 kg and it has a nominal maximum flight time of 45 minutes. The system incorporates a Cube Orange autopilot unit that is connected to two Here3 GNSS antennas, which enables real-time kinematic navigation capabilities when paired with a Here+ GNSS base station. The autopilot operates under the open-source ArduCopter flight controller and provides position and attitude data with a sampling frequency of 8 Hz.

2.2 The WindScanner system

The ground-based short-range WindScanner system developed by DTU Wind and Energy Systems consists of three synchronized coherent CW Doppler lidars (Fig. 3), which are capable of accurately retrieving wind vectors and measuring turbulence, see Sjöholm et al. (2009) for the original 3-inch system and Mikkelsen et al. (2020) for the newest system with 6-inch optics used in this investigation. The wedge-shaped dual-prism scanner heads enable the lidars to agilely and rapidly steer the laser beams in any direction within $\pm 61^\circ$ of the manually adjustable center axis (Mikkelsen et al., 2008). The focus position of the lidars can reach from about 20 m out to a few hundred meters, which can be easily changed by adjusting the distance between the optical fiber tip relative to the focus lens. Besides, the three lidars are synchronized by a central master computer, to scan the same commanded pattern in space simultaneously.

The detected backscatter signal by the lidars is mixed with the local oscillator and sampled at 120 MHz and the Fast Fourier Transform (FFT) frequency resolution becomes 234.4 kHz $=$ (120 MHz)/512 when Doppler spectra are calculated with 512 frequency bins. Consequently, the line-of-sight velocity bin resolution is 0.183 ms^{-1} $= (1.565\mu\text{m}/2) \cdot (234.4$ kHz), which is calculated by the FFT frequency resolution and the laser wavelength λ. After a block averaging of 726 spectra to reduce the noise fluctuation, the final spectra are sampled at a frequency of 322 Hz $=$ (120 MHz)/$(512 \cdot 726)$. Therefore, each lidar provides a data file with 19320 spectra for every minute of measurement. In addition, to distinguish the blue or red Doppler shift depending on whether the aerosols move towards or away from the lidar, the in-phase/quadrature-phase (IQ) homodyne detection method (Abari et al., 2014) is employed.

2.3 CFD simulations by Ansys

A total of seven CFD simulations by Ansys were conducted to compare with the experimental data. The design of the simulation relies on the study by Ghirardelli et al. (2023), where it is extensively described. The inflow wind speeds for this comparison were carefully adjusted to match the field experiment. The actual geometry of the drone is simplified according to the actuator disc theory (Rankine, 1865; Froude, 1889; Sayigh, 2012). The drone is treated as eight two-dimensional discs (Fig. 2a) that apply an instantaneous pressure jump in the flow, which are placed along the planes of rotation of the real drone propellers (0.71 m diameter). Disregarding the intricate details of each rotor blade's geometry has the advantage of reducing the real geometry mapping process and the computational time of the simulation. At the center of the actuator discs, there is a global reference point (0, 0, 0). The actuator discs are enclosed within a cubic volume domain that is 20D wide and tall, with a distance of 10D from each lateral side. Vertically, the center is located 7D from the top and 13D from the bottom. This disposition ensures that

https://doi.org/10.5194/egusphere-2023-1546
Preprint. Discussion started: 16 October 2023

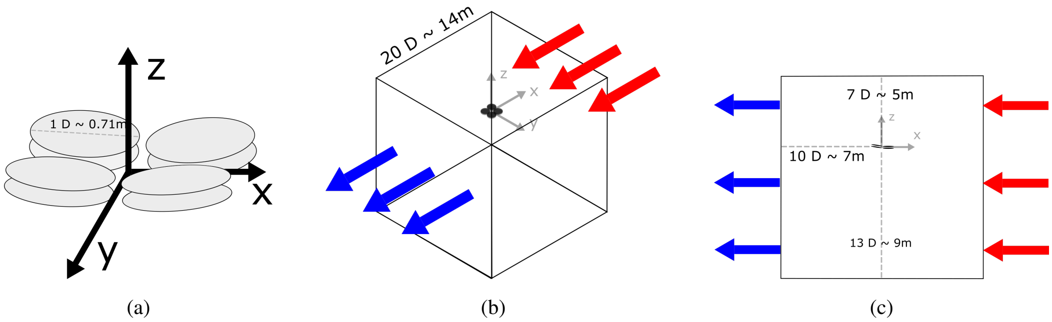

Figure 2. Schematic diagram of the computational domain with the flow entering through the inlet (red arrows), exiting through the outlet (blue arrows), and the remaining external faces considered as walls. **(a)** Eight actuator discs. **(b)** A three-dimensional isometric projection of the domain. **(c)** Side view.

the influence between the propeller-induced flow and the bottom wall is reduced. The wind speed is constant over the inflow plane.

The computational grid for the CFD simulations was automatically generated using Ansys Fluent Meshing with the Watertight Geometry workflow. This method simplifies mesh generation for CFD simulations, allowing users to perform all stages of the simulation, including meshing and post-processing, within a single software session and user interface (Ansys Fluent). The grid consists of a poly-hexcore mesh (Zore et al., 2019) and it was the subject of a mesh refinement study in Ghirardelli et al. (2023). To ensure accuracy, the maximum cell size within the domain was set to 0.3 m, while on the actuator discs, it was 0.02 m and overall, the grid comprises 1.66 million cells. The k-ϵ turbulence closure model is commonly used in CFD simulations for turbulent flows, especially in free-shear layer scenarios. It assumes fully turbulent flow and does not consider molecular viscosity effects. The selection of the k-ϵ model, instead of the k-omega and k-omega SST models, was based on the study's emphasis on non-wall flow characteristics. The setup parameters for the CFD simulations are summarized in Table 1.

3 Experimental setup

On the 14$^{\text{th}}$ and 15$^{\text{th}}$ of December 2022, we performed the field experiment with the WindScanner system at the Risø campus of the Technical University of Denmark (DTU), as depicted in Fig. 3. To shorten the probe lengths (Angelou et al., 2012), the three lidars were placed as close as possible to the intended scanning positions. Considering the lidars' shortest focus distance and a safe height from the drone to the reference met mast, the line-of-sight focus distance of the three lidars varied between 24.8 m and 30.9 m, with the corresponding elevation angle ranging from 42.3° to 27.8°. The probe length of each lidar or more precisely the full-width-at-half-maximum (FWHM) of the Lorentzian-shaped weighting function was in the range between 0.56 m and 0.87 m, which was calculated by

$$\mathrm{FWHM} = 2 \cdot z_R = 2 \cdot \frac{\lambda \cdot R^2}{\pi a_0^2} \tag{1}$$

https://doi.org/10.5194/egusphere-2023-1546
Preprint. Discussion started: 16 October 2023

Table 1. Summary of setup parameters of the CFD simulations and relative heights of the lidar scans. Flow above the drone is signified by positive Δh and vice versa flow below the drone by negative Δh. The yaw and tilt positions are also input to the simulation.

Measurement	Inlet Velocity U_0 (m/s)	Δh (m)	Yaw Angle (°)	Tilt Angle (°)
Plane Scans:	4.09	-0.7	21.2	2.7
	3.53	-2.1	26.4	2.8
	3.54	-3.7	14.0	2.9
	3.92	-4.5	34.4	3.3
Line Scans:	1.34	3.0	174.3	1.5
	1.51	2.2	174.2	1.6
	1.77	-1.6	354.3	1.4

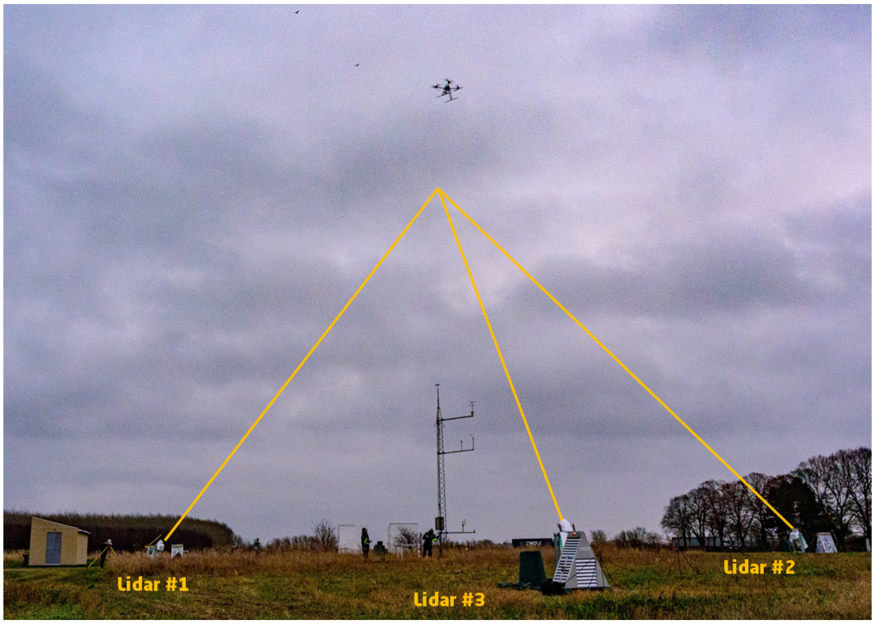

Figure 3. Experiment setup of the three CW Doppler lidars at DTU Risø campus. The surrounding terrain is relatively flat and agricultural. The three lidars focus at about 8 m above the top of a met mast.

where z_R is the Rayleigh length, $\lambda = 1.565$ μm the laser wavelength, R the distance from the lidar to where the beam is focused, and $a_0 = 33$ mm is the effective beam radius at the 6-inch lidar lens.

After focus calibration with a rotating hard target, the three lidars were programmed to scan synchronously a horizontal plane and a horizontal line, both centered above the met mast with a height distance of 8 m above its top. During measurements, we defined a right-handed coordinate system with the origin located at the reference point close to the bottom of the met mast,

https://doi.org/10.5194/egusphere-2023-1546
Preprint. Discussion started: 16 October 2023

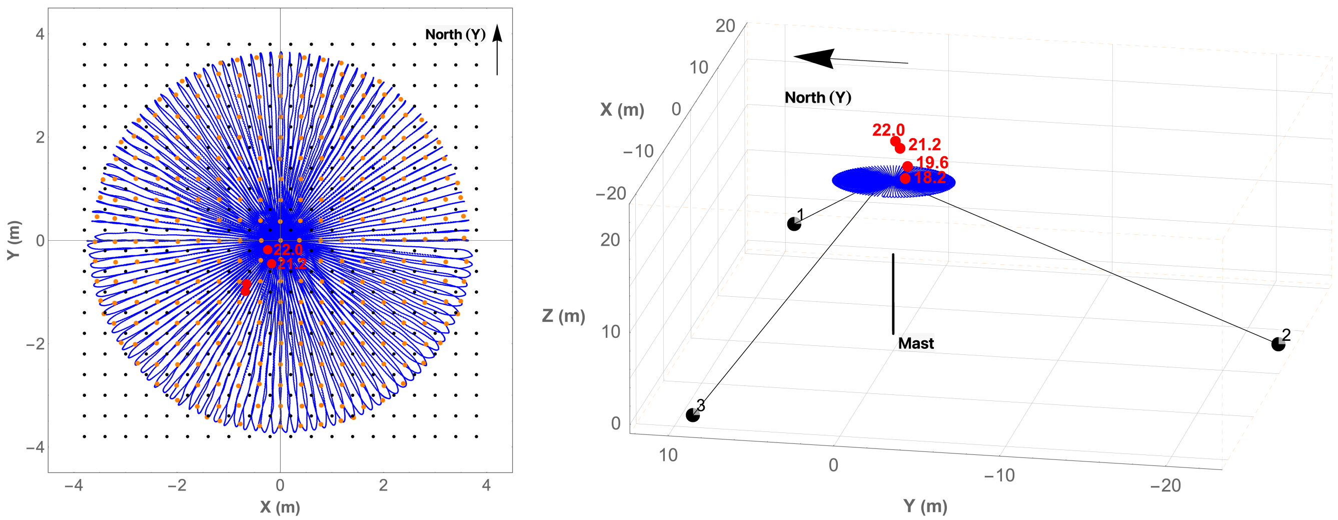

(a) (b)

Figure 4. The experimental setup for the plane scans. **(a)** Top-down view along the negative z-axis. **(b)** Side view. The three lidars are marked by numbers 1, 2, and 3, while the solid black line indicates the met mast. The scanning plane is at $z = 17.5$ m throughout the measurement campaign and the drone's average center positions and heights are indicated by the red dots. The black dots in **(a)** are the centers of the grid cells for grouping the scanning points, while the orange dots are the average measurement points in each cell.

the y-axis pointing towards the geographic north, the x-axis pointing east and z up (Fig. 4). The horizontal disc with a radius of 3.7 m was scanned using a trajectory of 60 horizontal 7.4 m long lines. The three laser beams followed a path that started from one side of the line, passed through the disc center to the other end of the line, and then returned over the same route to its starting point. The scanning duration of each horizontal line was 1 s, including the transition time to rotate 3° around the center of the line to the adjacent line. Therefore, the completion of the whole scanning plane took one minute.

During the horizontal plane scans lasting from 13:35 to 13:57 (all times mentioned in the paper are UTC+1), the drone hovered at four heights and stayed for five minutes at each height. The corresponding height difference Δh between the drone plane and the scanning plane is $\Delta h = -0.7$, -2.1, -3.7 and -4.5 m. The negative sign indicates that the scanning plane is below the drone. Fig. 4 shows the average drone positions for the four heights (red points). During the lidar measurement, the drone drifted southwest of the plane center, despite the intention to hover the drone at the center.

Similarly to the plane pattern, the cycle duration of the line scan was 1 s. In an attempt to align with the wind direction, the line spanned from $(x, y) = (-0.32, -3.62)$ m to $(+0.34, +3.64)$ m so it pointed approximately 5° anticlockwise from the north. This resulted in completing approximately 60 iterations of the line scan per minute. Line scans were performed by hovering the drone at three different heights close to the end of the line, as shown in Fig. 5. Consequently, the height difference Δh is 3.0, 2.2, and -1.6 m, and the horizontal orthogonal distance from the drone position to the scanning line in Fig. 5a is 0.2, 0.29, and 0.1 m.

https://doi.org/10.5194/egusphere-2023-1546
Preprint. Discussion started: 16 October 2023

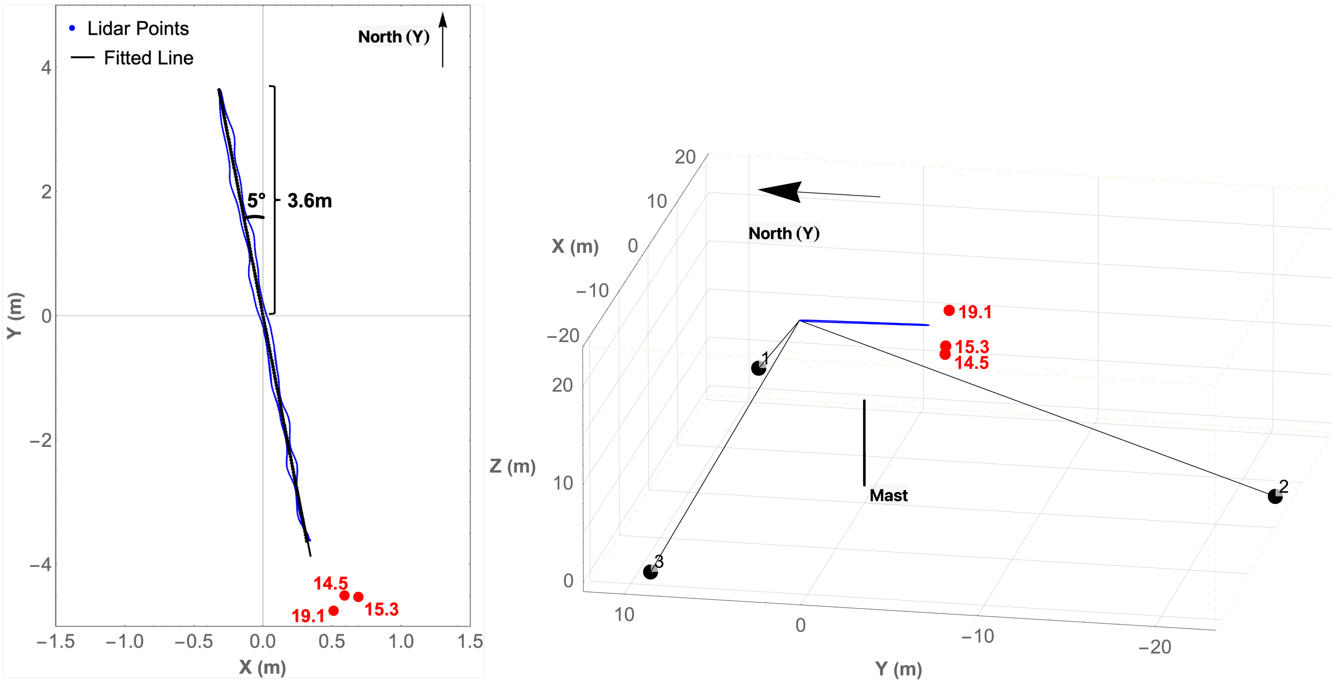

(a) (b)

Figure 5. The experimental setup for the line scans. **(a)** Top-down view along the negative z-axis. **(b)** Side view. The three lidars are marked by numbers 1, 2, and 3, while the solid black line in **(b)** indicates the met mast. The measurements were taken at a height of 17.5 m, the same as the plane scan. The black line in **(a)** is the fitted scanning line.

The 10-minute wind characteristics measured by sonic and cup anemometers 18 m a.g.l. on the met mast west of the DTU V52 wind turbine (358 m north to the met mast in Fig. 3) are presented in Fig. 6. Sonic anemometer measurements indicated that the average horizontal wind velocity for the plane scans was $3.44\ \mathrm{ms}^{-1}$, while it was $2.11\ \mathrm{ms}^{-1}$ for the line scans. The 10-minute wind direction was from $-22.7°$ (northwest) during the plane scans and later changed to $9.95°$ (northeast) for the line scans. Additionally, the 10-minute vertical wind component varied from -0.13 to $-0.17\ \mathrm{ms}^{-1}$ during the measurement period. As shown in Fig. 6, the average wind speed and direction obtained from the three lidars far from the drone are represented by green dots. Even if there are some differences, it is a good comparison since the lidars and the sonic anemometer are relatively far apart (358 m).

4 Post-processing and data analysis

A relatively stable estimate of the flow around the drone could be made after 3 minutes corresponding to 3 iterations of the plane scanning. The data acquired for the plane scan was grouped by the index of every square grid cell, which has a dimension of 0.4×0.4 m (the black dots in Fig. 4a). Hence, with a scanning step of 4.7 cm and a spectral sampling frequency of 322 Hz from the lidars, at least 50 Doppler spectra were present in each grid cell. Analysis of the line scan was performed using

https://doi.org/10.5194/egusphere-2023-1546
Preprint. Discussion started: 16 October 2023

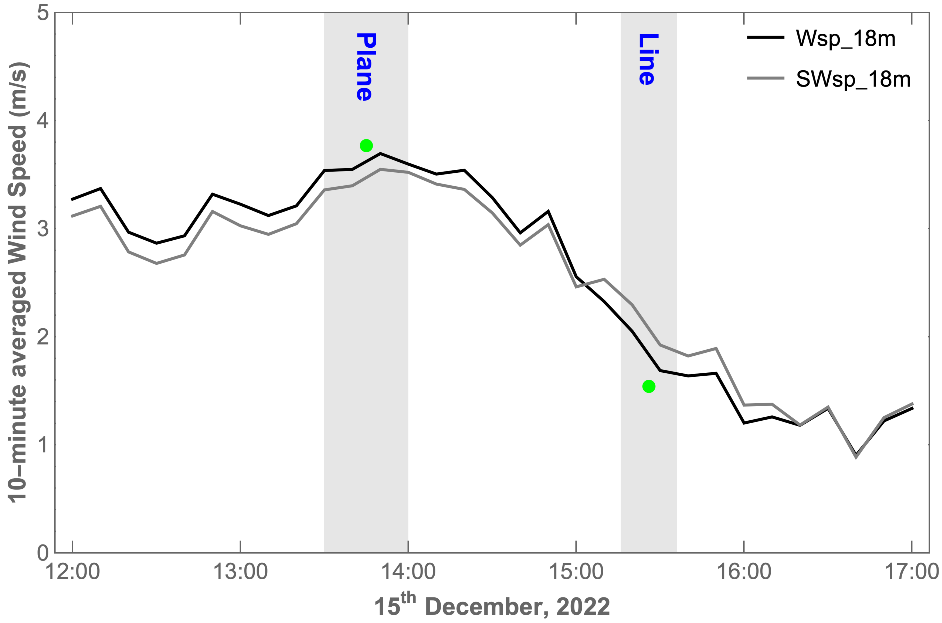

(a)

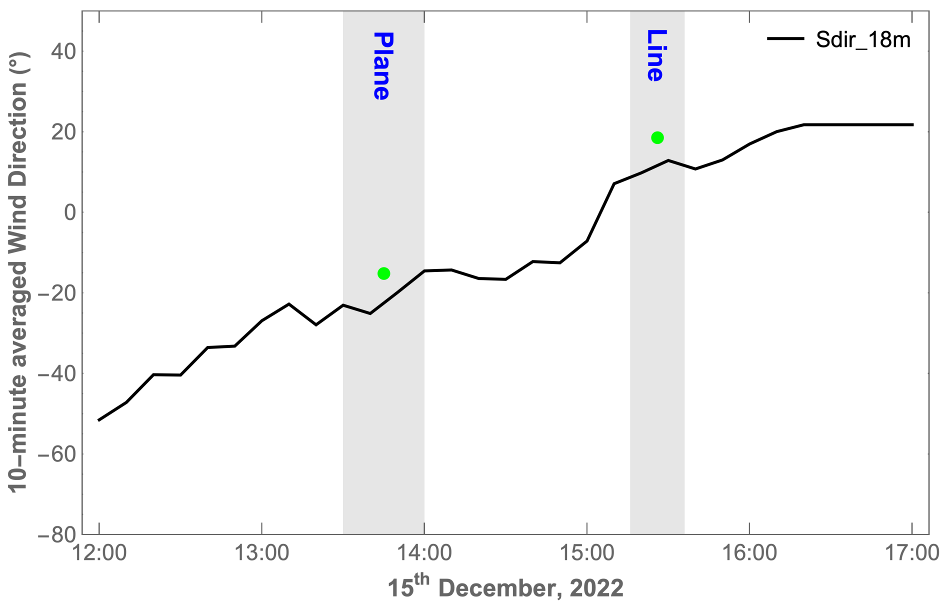

(b)

Figure 6. 10-minute wind measurements by sonic and cup anemometers at 18 m height. **(a)** Wind speed measured by the sonic (SWsp) and cup (Wsp) anemometers. **(b)** Wind direction measured by the sonic anemometer (Sdir). The gray bars mark the plane scan period from 13:35 to 13:57 (UTC+1) and the line scan period from 15:16 to 15:36 (UTC+1). The green dots are the corresponding measurements by the lidars.

one-minute lidar data consisting of 60 iterations of the line cycle. We segmented the line every 5 cm, resulting in at least 120 Doppler spectra per segment.

After the Doppler spectra were processed with the steps of dividing raw spectra with the background noise, subtracting a spectral threshold, and replacing negative values with zeros, they were averaged in the same grid cell or segment. Thereafter, we applied the median method (the median of the accumulated energy in the spectrum) to calculate the line-of-sight wind velocity (Held and Mann, 2018), and retrieved the wind vectors based on the line-of-sight velocities determined from the three lidars.

Despite placing the three lidars as close as possible to minimize the probe length, they could still hit the drone body or the rotational propellers during measurement. As demonstrated in Fig. 7b, the Doppler signal appearing at the center of the spectrum is caused by the drone body, while the signal on the left side marked by the red arrow is induced by the propeller. Compared with the normal Doppler signal caused by the aerosols in Fig. 7a, the energy of the two peaks in Fig. 7b is much higher because of the reflected light from the hard targets. By adding up the power spectral density we can easily identify an area for each lidar where beams hit either the drone body or its propellers, see Fig. 7c and d. With an increasing height difference Δh, the strong backscatter area moves away from the drone center, as seen from Fig. 7d. Consequently, we filter out the Doppler spectra whose sum exceeds a certain threshold to eliminate the detrimental effects of hard targets.

For better comparison with the flow field by CFD simulations, the xyz coordinate was rotated to align the free flow direction with the north. Subsequently, the three-dimensional wind vector components U, V, W were retrieved from the three simultaneously measured radial wind velocity v_1, v_2, v_3 by lidars and a unit vector $\boldsymbol{n}$ (Mann et al., 2009). The retrieval is done by

$$\begin{bmatrix} U \\ V \\ W \end{bmatrix} = \begin{bmatrix} \cos\alpha & \sin\alpha & 0 \\ -\sin\alpha & \cos\alpha & 0 \\ 0 & 0 & 1 \end{bmatrix} \cdot \begin{bmatrix} \boldsymbol{n_1} \\ \boldsymbol{n_2} \\ \boldsymbol{n_3} \end{bmatrix}^{-1} \cdot \begin{bmatrix} v_1 \\ v_2 \\ v_3 \end{bmatrix} \tag{2}$$

where $\boldsymbol{n_1}$, $\boldsymbol{n_2}$, $\boldsymbol{n_3}$ are the unit vectors of the three lidars in the direction of the lidar beam, which is conventionally negative if away from the lidar, α is the polar angle from north toward the inflow wind direction (positive counterclockwise if seen from above). In the end, the coordinate was rotated $270°$ counterclockwise to align the positive x-axis with the free flow direction.

5 Results

5.1 The flow field in a horizontal plane below the drone

The 3-minute-averaged downwash flow in a horizontal plane simulated by CFD and retrieved by the three lidars is exhibited in Fig. 8 while the drone was hovering at 0.7 meters above the scanning plane. The free wind speed was $4.09\ \mathrm{ms}^{-1}$ along the positive x-axis and the drone was yawed about $21.2°$ to the incoming wind. In general, the flow patterns predicted by the CFD simulations and the lidar measurements are consistent.

https://doi.org/10.5194/egusphere-2023-1546
Preprint. Discussion started: 16 October 2023

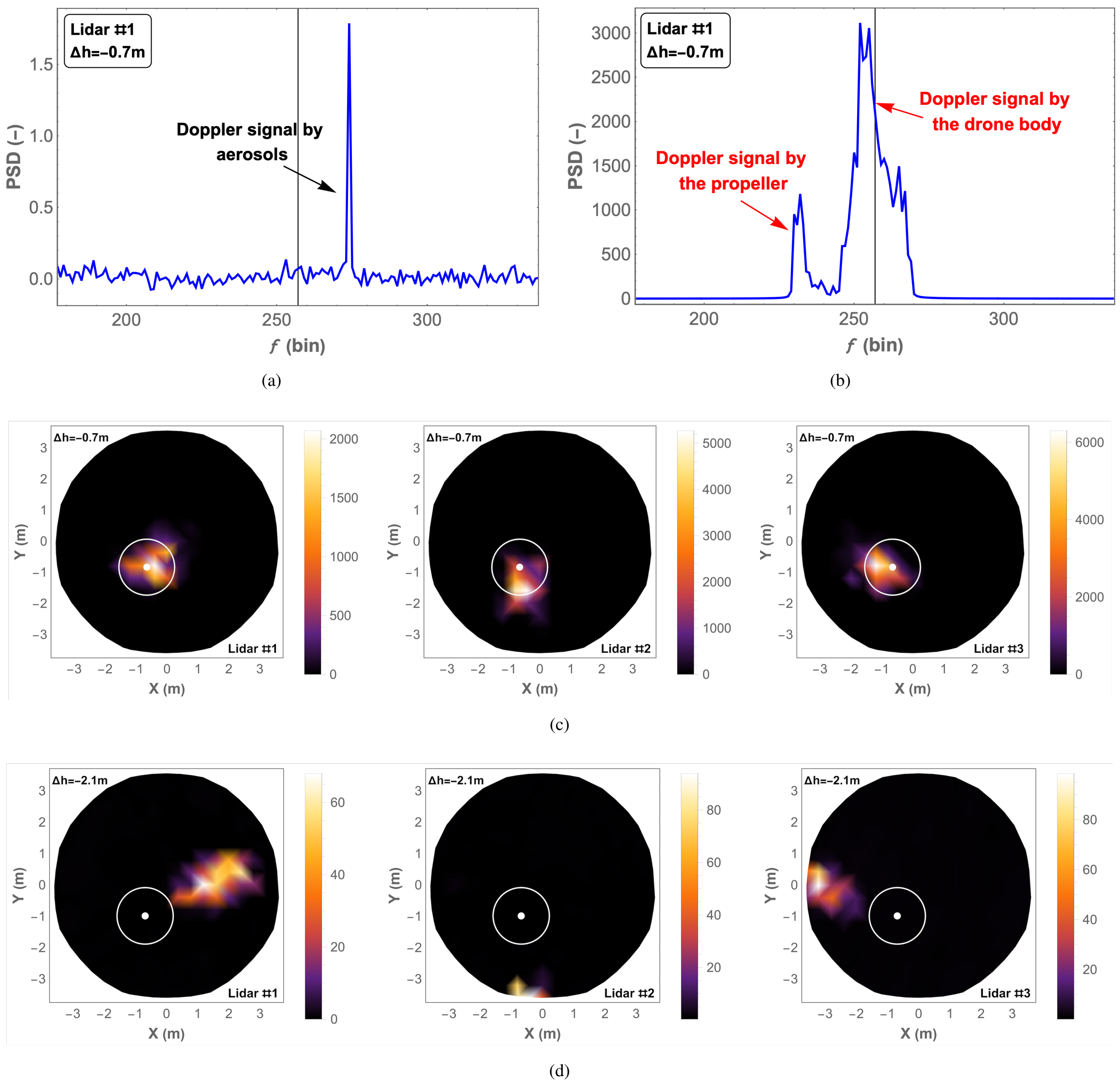

Figure 7. Examples of representative Doppler spectra and the sum of the power spectral density (PSD) within a reasonable frequency range where the Doppler signal occurs. **(a)** Noise-flattened spectrum containing only aerosol-induced Doppler signal. **(b)** Noise-flattened spectrum containing the Doppler signal caused by the drone. **(c)** Sum of PSD at $\Delta h = -0.7$ m. **(d)** Sum of PSD at $\Delta h = -2.1$ m. The white dot and circle are the drone center and diameter seen from above.

https://doi.org/10.5194/egusphere-2023-1546
Preprint. Discussion started: 16 October 2023

For a clearer illustration, we normalized the horizontal wind velocity $\sqrt{U^2+V^2}$ by subtracting the free wind speed U_0. Fig. 8a and b clearly illustrate how a blockage effect in the upstream induction zone slows the free wind velocity and the accelerated flow beside the downstream drone wake. According to Fig. 8c and d, the flow transverse to the inflow wind diverges upstream of the drone and converges downstream. The vertical velocity W in Fig. 8e and f has a peak value of 12 ms^{-1} in the CFD simulations and 5.4 ms^{-1} in the observations, respectively. It should be noted, however, that lidar measurements did not capture the very detailed flow feature due to the averaging effect of lidars' measurement volume and the drone drifting approximately ± 0.5 m along the free flow direction from its average position (the central black dot in Fig. 8).

Additionally, CFD simulations and lidar measurements indicate that the disturbance zone in horizontal wind velocity, defined as more than 1% difference relative to the free wind, extends about 2 meters upstream from the drone. However, in terms of vertical wind velocity in Fig. 8e and f, it stretches more than 5 meters.

A comparison of wind speed obtained by the CFD simulations and lidar measurements is depicted in Fig. 9, where the drone was hovering at the three different heights displayed in Fig. 4. As the drone moves upwards increasing the distance to the scanning plane, both CFD simulations and lidar measurements show that the high-speed downwash is pushed downstream. When the drone was hovering at 2.1 m above the plane, the accelerated area after the drone measured by the lidars was less prominent compared to the CFD simulations in Fig. 9c. This is probably due to the aforementioned averaging effect of lidars and the drones' drifting. For the last two heights as $\Delta h = -3.7$ m and -4.5 m (not shown), the drone's downwash flow has no significant impact in the shown area.

5.2 The flow field on horizontal lines around a drone

In addition to the measurement in a horizontal plane, the turbulent flow around the drone was also measured with upstream horizontal lines starting about 0.9 meters upstream from the drone center in Fig. 10, while the drone was hovering at three heights (Fig. 5) and drifting around the average position within a radius of less than 25 cm. The averaged wind velocities over a period of 1 minute are presented in Fig. 11. A good agreement can be observed between the CFD simulations and lidar measurements for horizontal and vertical wind velocities, with differences of only about 0.1 ms^{-1} at all three heights studied, except for the vertical velocity W at $\Delta h = -1.6$ m, which differs by 0.2 ms^{-1}. Several factors contribute to these differences. The simulations are conducted with laminar inflow without turbulent fluctuations, which is not the case in reality. Besides, the propellers are simplified based on the actuator disc theory, limiting the ability to accurately estimate the flow, especially when it comes to the turbulence generated by the real propellers. Lastly, the averaging effect of lidars' measurement volume also leads to differences with simulations.

At all three heights, both methods yield about a nearly zero transverse velocity V (not shown). It is also clearly demonstrated in Fig. 11 that there is a decrease in the horizontal wind velocity in the induction zone with $\Delta h < 0$, as well as an acceleration in the area above the drone with $\Delta h > 0$. The CFD simulations and lidar measurements agree well in the area that is most relevant for placing anemometers, both for plane and line scans. Consequently, CFD simulations can be a reliable, convenient, and affordable approach to studying complex flow around drones under different flow conditions.

https://doi.org/10.5194/egusphere-2023-1546
Preprint. Discussion started: 16 October 2023

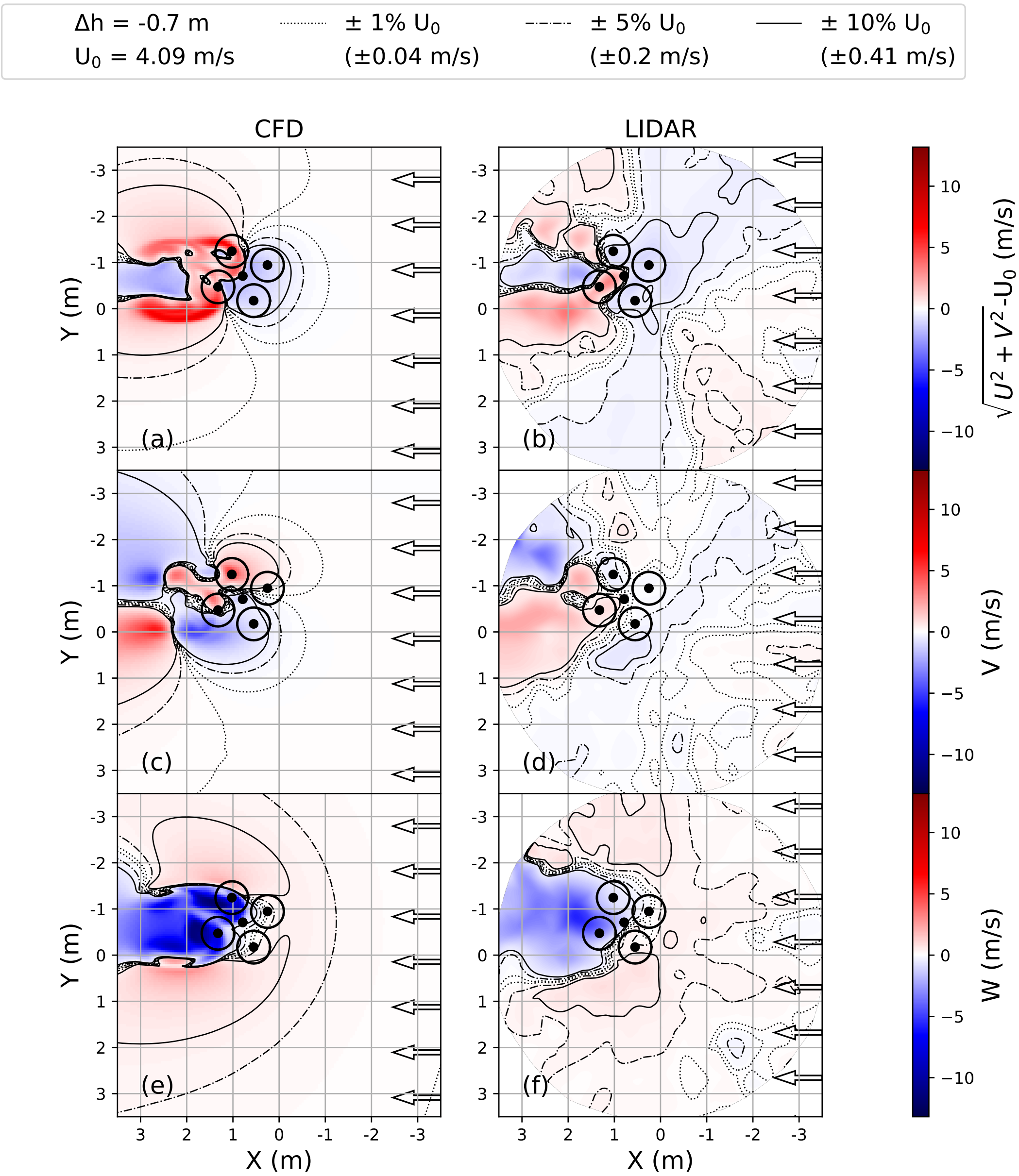

Figure 8. A comparison of wind fields and velocity contours of 1%, 5%, and 10% deviation from U_0 obtained by CFD simulations (left column) and 3-minute-averaged lidar data (right column) in a horizontal plane with the drone about 0.7 m above. Four circles represent the drone propellers and the black dot out of the circles is the average drone center.

https://doi.org/10.5194/egusphere-2023-1546
Preprint. Discussion started: 16 October 2023

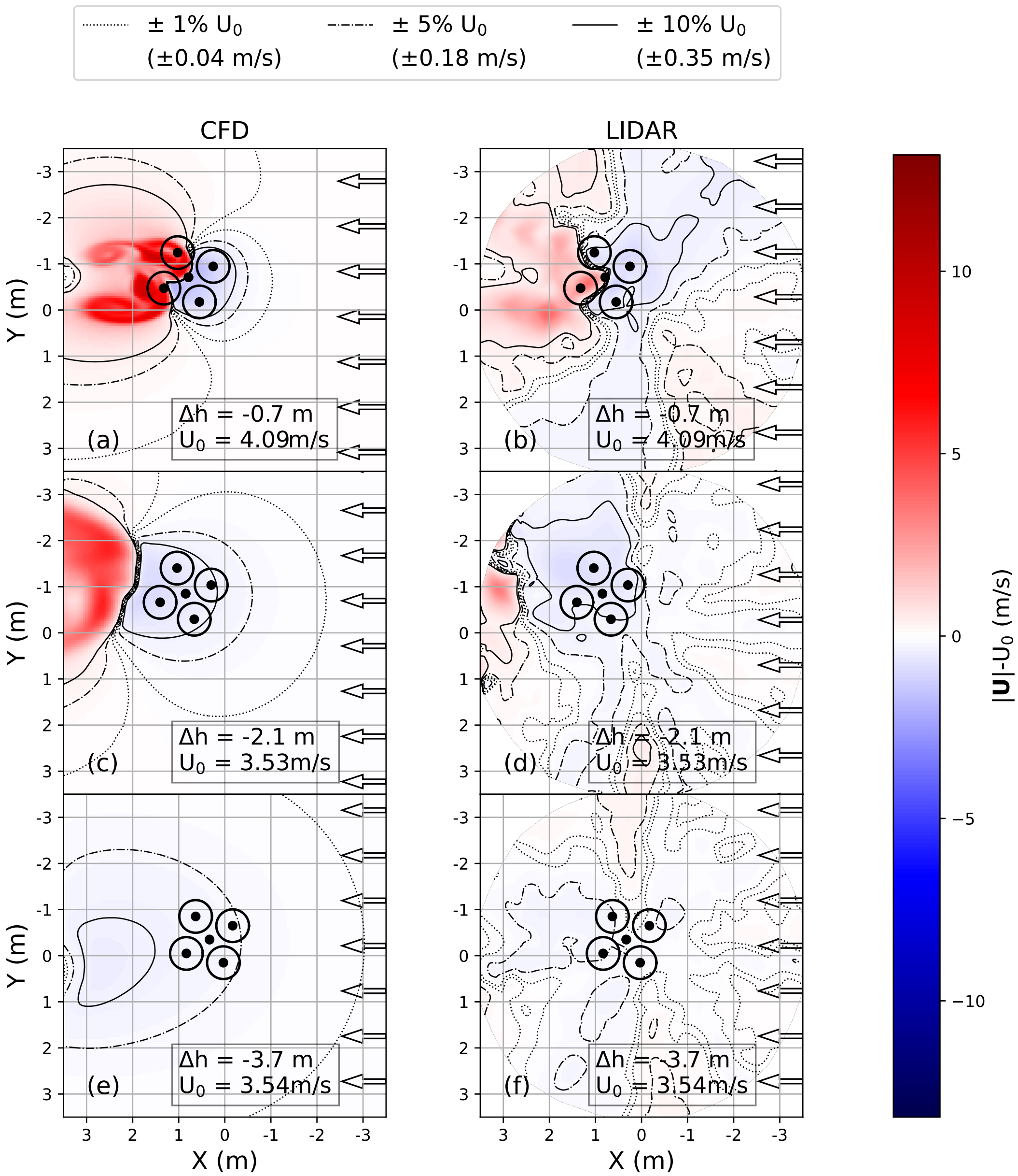

Figure 9. A comparison of wind speed $|\boldsymbol{U}|$ and speed contours of 1%, 5%, and 10% deviation from U_0 obtained by CFD simulations (left column) and 3-minute-averaged lidar data (right column) in a horizontal plane, while the drone was hovering at 0.7 m, 2.1 m, and 3.7 m above the plane. Four circles represent the drone propellers and the black dot between the circles is the average drone center.

https://doi.org/10.5194/egusphere-2023-1546
Preprint. Discussion started: 16 October 2023

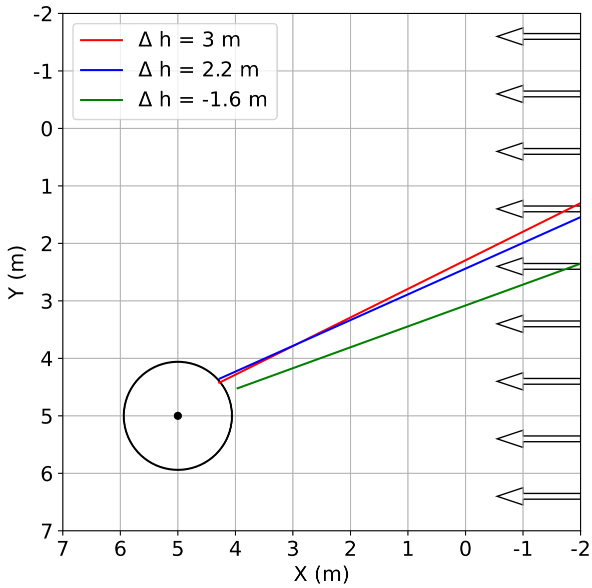

Figure 10. A top-down view of line scans after the coordinate has been centered at the average drone center (black dot) with the drone about 3 m and 2.2 m below and 1.6 m above the line. The black circle represents the drone's diameter of 1.88 m.

Based on the aforementioned conclusions, we display the flow patterns on a vertical plane by CFD simulations with the lowest free wind speed of $1.3\ \mathrm{ms}^{-1}$ in Fig. 12. We chose to show a small free wind speed because that is where the upstream flow is mostly affected by the drone (Wen et al., 2019). The stronger the wind, the more tilted the downwash will be. When a sonic anemometer is placed 0 m below the drone, the horizontal distance should be 4.8 m upstream to achieve less than $\pm 5\%$ distortion of both horizontal and vertical wind velocities at lower ambient speed.

6 Conclusions and discussions

Three ground-based continuous-wave Doppler lidars with high spatial and temporal resolution have been applied to characterize the turbulent flow induced by a rotary-wing drone hovering at different heights. Through the synchronization of the three lidars, two scanning scenarios were designed: plane scanning and line scanning. The wind fields retrieved by the lidars were compared with those obtained from the CFD simulations. Both plane and line scans show a good agreement with simulations.

For plane scans, the lidar measurements and CFD simulations show similar flow patterns. In the case of the plane scan at 0.7 meters below the drone, both methods demonstrate that the disturbance zone for the horizontal wind velocity stretches 2 meters from the drone center and more than 5 meters for the vertical velocity component. However, the CFD simulations show larger drone-induced peak velocity deviations from the free flow than the lidar does, which can be understood by considering the lidar's averaging effect and the smearing by the drone's random drift. Additionally, the line scans show that the velocity

https://doi.org/10.5194/egusphere-2023-1546
Preprint. Discussion started: 16 October 2023

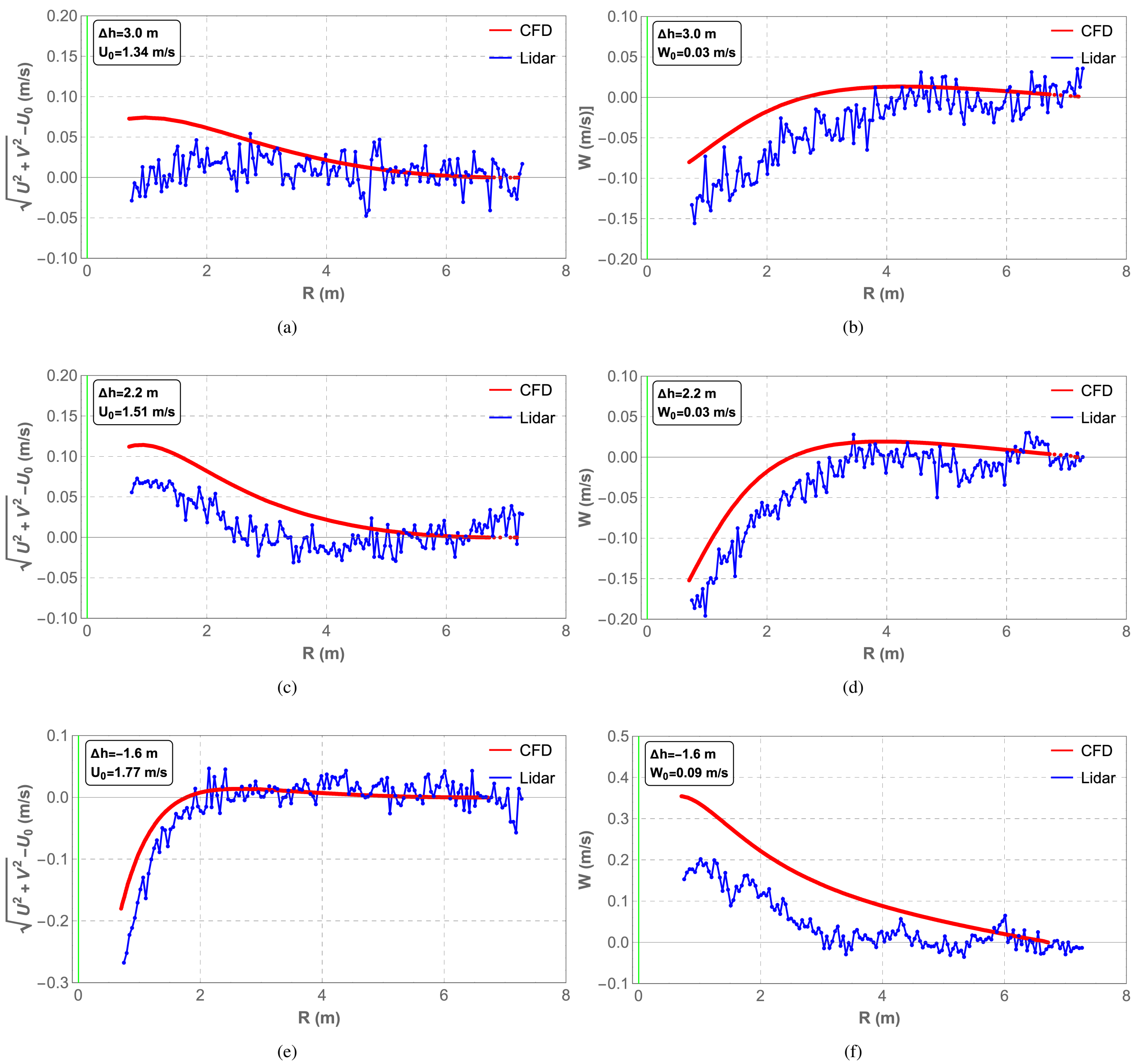

Figure 11. Comparison of wind velocities between CFD simulations and 1-minute-averaged lidar data along the scanning line with the drone about 3 m and 2.2 m below and 1.6 m above the line. **(a)**, **(c)**, and **(e)** Normalized horizontal wind velocity. **(b)**, **(d)**, and **(f)** Vertical wind velocity. The green line indicates the average drone position.

https://doi.org/10.5194/egusphere-2023-1546
Preprint. Discussion started: 16 October 2023

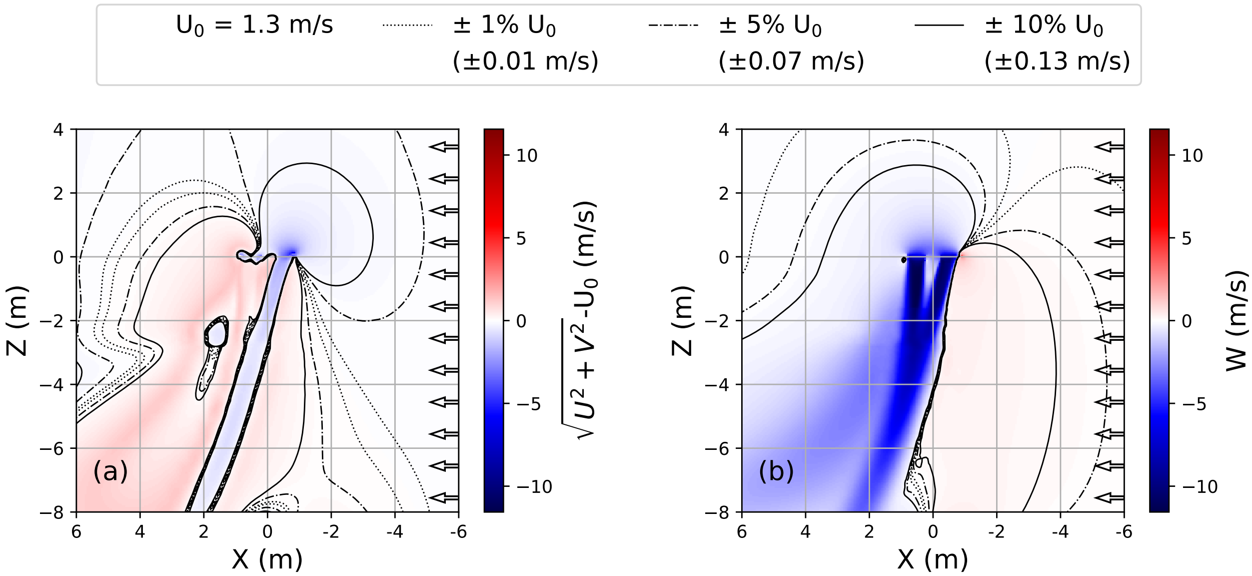

Figure 12. Flow patterns and velocity contours of 1%, 5%, and 10% deviation from $U_0 = 1.3\mathrm{ms}^{-1}$ on cross-sections over the xz-plane by CFD simulations. **(a)** Normalized horizontal wind velocity. **(b)** Vertical wind velocity.

difference between the two methods is less than 0.2 ms^{-1} at low ambient wind speeds. These facts validate that the CFD methodology presented in this study can be used as an investigative tool for positioning drone-mounted anemometers.

To achieve both accurate horizontal and vertical wind velocity measurements, the optimal drone-mounted sonic position should be at least 5 meters upstream from the drone center at low ambient wind speeds based on the CFD simulations. However, if only horizontal velocity is of interest, this distance will be significantly shortened. From this study, we concluded that it is difficult to measure vertical wind velocity precisely (less than 1% distortion) with drone-mounted sonic anemometers. Further investigations could include flying the drone at higher free wind speeds and mounting a sonic anemometer on the drone in the upstream direction to validate the potentially optimal position defined by the simulations.

Data availability. Data underlying the results presented in this paper can be obtained from the authors upon reasonable request.

Author contributions. All authors have made a contribution to the paper preparation. Conceptualization, JM, JR, MS; methodology, project management, and experiment conduction, LJ, MG, JM, MS, JR, SK; data analysis, LJ, MG; writing—original draft preparation, LJ, MG; writing—review and editing, LJ, MG, JM, MS, JR, SK. All authors have read and agreed to the published version of the manuscript.

https://doi.org/10.5194/egusphere-2023-1546
Preprint. Discussion started: 16 October 2023

Competing interests. The authors declare no conflict of interest.

Acknowledgements. The authors would like to thank Michael Courtney, Per Hansen, Lars Christensen, Michael Rasmussen, and Claus Brian Munk Pedersen from DTU, for their helpful support during the field experiment, fruitful discussions, and helpful comments.

Financial support. This research is mainly funded by the two Marie Sklodowska Curie Innovation Training Networks LIKE (H2020-MSCA-ITN-2019, Grant number 858358), and Train2Wind (H2020-MSCA-ITN-2019, Grant number 861291). Additional funding comes from Atmospheric FLow, Loads, and pOwer for Wind energy (FLOW, HORIZON-CL5-2021-D3-03-04, Grant number 101084205), funded by the European Union.

https://doi.org/10.5194/egusphere-2023-1546
Preprint. Discussion started: 16 October 2023

References

Abari, C. F., Pedersen, A. T., and Mann, J.: An all-fiber image-reject homodyne coherent Doppler wind lidar, Optics express, 22, 25 880–25 894, 2014.

Abichandani, P., Lobo, D., Ford, G., Bucci, D., and Kam, M.: Wind measurement and simulation techniques in multi-rotor small unmanned aerial vehicles, IEEE Access, 8, 54 910–54 927, 2020.

Angelou, N., Mann, J., Sjöholm, M., and Courtney, M.: Direct measurement of the spectral transfer function of a laser based anemometer, Review of scientific instruments, 83, 033 111, 2012.

Angelou, N., Mann, J., and Dellwik, E.: Wind lidars reveal turbulence transport mechanism in the wake of a tree, Atmospheric Chemistry and Physics, 22, 2255–2268, 2022.

Ansys Fluent: Watertight Geometry workflow, https://www.ansys.com/training-center/course-catalog/fluids/ansys-fluent-meshing-with-watertight-geometry-workflow, accessed: 2023-06-28.

Bingöl, F., Mann, J., and Foussekis, D.: Conically scanning lidar error in complex terrain, Meteorologische Zeitschrift, pp. 189–195, 2009.

Bos, R., Giyanani, A., and Bierbooms, W.: Assessing the severity of wind gusts with lidar, Remote Sensing, 8, 758, 2016.

Bowen, B.: Improved wind and turbulence measurements using a low-cost 3-D sonic anemometer at a low-wind site, Tech. rep., Lawrence Livermore National Lab.(LLNL), Livermore, CA (United States), 2007.

Cheynet, E., Jakobsen, J. B., Snæbjörnsson, J., Mikkelsen, T., Sjöholm, M., Mann, J., Hansen, P., Angelou, N., and Svardal, B.: Application of short-range dual-Doppler lidars to evaluate the coherence of turbulence, Experiments in Fluids, 57, 1–17, 2016.

Fan, Z., Li, S., Gao, Z., Zhang, L., Zheng, X., Zhu, W., Shen, W., Sjöholm, M., Mikkelsen, T. K., Wang, T., et al.: On the importance of wind turbine wake boundary to wind energy and environmental impact, Energy Conversion and Management, 277, 116 664, 2023.

Froude, R. E.: On the part played in propulsion by differences of fluid pressure, Trans. Inst. Naval Architects, 30, 390, 1889.

Ghirardelli, M., Kral, S. T., Müller, N. C., Hann, R., Cheynet, E., and Reuder, J.: Flow Structure around a Multicopter Drone: A Computational Fluid Dynamics Analysis for Sensor Placement Considerations, Drones, 7, https://doi.org/10.3390/drones7070467, 2023.

Guillermo, P. H., Daniel, A. V., and Eduardo, G. E.: CFD Analysis of two and four blades for multirotor Unmanned Aerial Vehicle, in: 2018 IEEE 2nd Colombian Conference on Robotics and Automation (CCRA). IEEE, pp. 1–6, 2018.

Guo, F., Mann, J., Peña, A., Schlipf, D., and Cheng, P. W.: The space-time structure of turbulence for lidar-assisted wind turbine control, Renewable Energy, 195, 293–310, 2022.

Guo, Q., Zhu, Y., Tang, Y., Hou, C., He, Y., Zhuang, J., Zheng, Y., and Luo, S.: CFD simulation and experimental verification of the spatial and temporal distributions of the downwash airflow of a quad-rotor agricultural UAV in hover, Computers and Electronics in Agriculture, 172, 105 343, 2020.

Held, D. P. and Mann, J.: Comparison of methods to derive radial wind speed from a continuous-wave coherent lidar Doppler spectrum, Atmospheric Measurement Techniques, 11, 6339–6350, 2018.

Hemingway, B. L., Frazier, A. E., Elbing, B. R., and Jacob, J. D.: Vertical sampling scales for atmospheric boundary layer measurements from small unmanned aircraft systems (sUAS), Atmosphere, 8, 176, 2017.

Izumi, Y. and Barad, M. L.: Wind speeds as measured by cup and sonic anemometers and influenced by tower structure, Journal of Applied Meteorology and Climatology, 9, 851–856, 1970.

Kaimal, J., Wyngaard, J., and Haugen, D.: Deriving power spectra from a three-component sonic anemometer, Journal of Applied Meteorology and Climatology, 7, 827–837, 1968.

https://doi.org/10.5194/egusphere-2023-1546
Preprint. Discussion started: 16 October 2023

Köpp, F., Schwiesow, R., and Werner, C.: Remote measurements of boundary-layer wind profiles using a CW Doppler lidar, Journal of Applied Meteorology and Climatology, 23, 148–154, 1984.

Lazard, N.: Lazard's Levelized Cost of Energy Analysis—Version 13.0, 2019.

Lei, Y. and Cheng, M.: Aerodynamic performance of a Hex-rotor unmanned aerial vehicle with different rotor spacing, Measurement and Control, 53, 711–718, 2020.

Lei, Y. and Lin, R.: Effect of wind disturbance on the aerodynamic performance of coaxial rotors during hovering, Measurement and Control, 52, 665–674, 2019.

Lei, Y., Ye, Y., and Chen, Z.: Horizontal wind effect on the aerodynamic performance of coaxial Tri-Rotor MAV, Applied Sciences, 10, 8612, 2020.

Leuenberger, D., Haefele, A., Omanovic, N., Fengler, M., Martucci, G., Calpini, B., Fuhrer, O., and Rossa, A.: Improving high-impact numerical weather prediction with lidar and drone observations, Bulletin of the American Meteorological Society, 101, E1036–E1051, 2020.

Li, Z., Pu, O., Pan, Y., Huang, B., Zhao, Z., and Wu, H.: A Study on Measuring the Wind Field in the Air Using a multi-rotor UAV Mounted with an Anemometer, Boundary-Layer Meteorology, 188, 1–27, 2023.

Luderer, G., Pietzcker, R. C., Carrara, S., de Boer, H. S., Fujimori, S., Johnson, N., Mima, S., and Arent, D.: Assessment of wind and solar power in global low-carbon energy scenarios: an introduction, Energy Economics, 64, 542–551, 2017.

MacCready, P. B.: Mean wind speed measurements in turbulence, Journal of Applied Meteorology (1962-1982), 5, 219–225, 1966.

Mann, J., Cariou, J.-P., Courtney, M. S., Parmentier, R., Mikkelsen, T., Wagner, R., Lindelow, P., Sjoholm, M., and Enevoldsen, K.: Comparison of 3D turbulence measurements using three staring wind lidars and a sonic anemometer, Meteorologische Zeitschrift, 18, 135, 2009.

Mikkelsen, T., Mann, J., Courtney, M., and Sjöholm, M.: Windscanner: 3-D wind and turbulence measurements from three steerable doppler lidars. IOP Conf, Ser. Earth Environ. Sci, 1, 1755–1315, 2008.

Mikkelsen, T., Sjöholm, M., Astrup, P., Peña, A., Larsen, G., Van Dooren, M., and Sekar, A. K.: Lidar Scanning of Induction Zone Wind Fields over Sloping Terrain, in: Journal of Physics: Conference Series, vol. 1452, p. 012081, IOP Publishing, 2020.

Peña, A., Hasager, C. B., Gryning, S.-E., Courtney, M., Antoniou, I., and Mikkelsen, T.: Offshore wind profiling using light detection and ranging measurements, Wind Energy: An International Journal for Progress and Applications in Wind Power Conversion Technology, 12, 105–124, 2009.

Prudden, S., Fisher, A., Mohamed, A., and Watkins, S.: A flying anemometer quadrotor: Part 1, in: Proceedings of the International Micro Air Vehicle Conference (IMAV 2016), Beijing, China, pp. 17–21, 2016.

Rankine, W. J. M.: On the mechanical principles of the action of propellers, Transactions of the Institution of Naval Architects, 6, 1865.

Sayigh, A.: Comprehensive Renewable Energy, vol. 2, Elsevier, 2012.

Sempreviva, A. M., Barthelmie, R. J., and Pryor, S.: Review of methodologies for offshore wind resource assessment in European seas, Surveys in Geophysics, 29, 471–497, 2008.

Shimura, T., Inoue, M., Tsujimoto, H., Sasaki, K., and Iguchi, M.: Estimation of wind vector profile using a hexarotor unmanned aerial vehicle and its application to meteorological observation up to 1000 m above surface, Journal of Atmospheric and Oceanic Technology, 35, 1621–1631, 2018.

Shin, D. and Ko, K.: Application of the nacelle transfer function by a nacelle-mounted light detection and ranging system to wind turbine power performance measurement, Energies, 12, 1087, 2019.

https://doi.org/10.5194/egusphere-2023-1546
Preprint. Discussion started: 16 October 2023

Sjöholm, M., Mikkelsen, T., Mann, J., Enevoldsen, K., and Courtney, M.: Spatial averaging-effects on turbulence measured by a continuous-wave coherent lidar, Meteorologische Zeitschrift (Berlin), 18, 2009.

Sjöholm, M., Angelou, N., Hansen, P., Hansen, K. H., Mikkelsen, T., Haga, S., Silgjerd, J. A., and Starsmore, N.: Two-dimensional rotorcraft downwash flow field measurements by lidar-based wind scanners with agile beam steering, Journal of Atmospheric and Oceanic Technology, 31, 930–937, 2014.

Thielicke, W., Hübert, W., Müller, U., Eggert, M., and Wilhelm, P.: Towards accurate and practical drone-based wind measurements with an ultrasonic anemometer, Atmospheric Measurement Techniques, 14, 1303–1318, 2021.

Tikhomirov, A. B., Lesins, G., and Drummond, J. R.: Drone measurements of surface-based winter temperature inversions in the High Arctic at Eureka, Atmospheric Measurement Techniques, 14, 7123–7145, 2021.

Vasiljević, N., Harris, M., Tegtmeier Pedersen, A., Rolighed Thorsen, G., Pitter, M., Harris, J., Bajpai, K., and Courtney, M.: Wind sensing with drone-mounted wind lidars: proof of concept, Atmospheric Measurement Techniques, 13, 521–536, 2020.

Viselli, A., Filippelli, M., Pettigrew, N., Dagher, H., and Faessler, N.: Validation of the first LiDAR wind resource assessment buoy system offshore the Northeast United States, Wind Energy, 22, 1548–1562, 2019.

Wagner, R., Pedersen, T. F., Courtney, M., Antoniou, I., Davoust, S., and Rivera, R.: Power curve measurement with a nacelle mounted lidar, Wind Energy, 17, 1441–1453, 2014.

Wen, S., Han, J., Ning, Z., Lan, Y., Yin, X., Zhang, J., and Ge, Y.: Numerical analysis and validation of spray distributions disturbed by quad-rotor drone wake at different flight speeds, Computers and Electronics in Agriculture, 166, 105 036, 2019.

Wilson, T. C., Brenner, J., Morrison, Z., Jacob, J. D., and Elbing, B. R.: Wind speed statistics from a small uas and its sensitivity to sensor location, Atmosphere, 13, 443, 2022.

Zhang, L. and Yang, Q.: A method for yaw error alignment of wind turbine based on LiDAR, IEEE Access, 8, 25 052–25 059, 2020.

Zheng, Y., Yang, S., Liu, X., Wang, J., Norton, T., Chen, J., and Tan, Y.: The computational fluid dynamic modeling of downwash flow field for a six-rotor UAV, Frontiers of Agricultural Science and Engineering, 5, 159–167, 2018.

Zore, K., Sasanapuri, B., Parkhi, G., and Varghese, A.: Ansys mosaic poly-hexcore mesh for high-lift aircraft configuration, in: 21st AeSI Annual CFD Symposium, 2019.